

Tetragonal and collapsed-tetragonal phases of CaFe_2As_2 : A view from angle-resolved photoemission and dynamical mean-field theory

Ambroise van Roeyghem,^{1,2,*} Pierre Richard,^{1,3} Xun Shi,^{1,4} Shangfei Wu,¹ Lingkun Zeng,¹ Bayrammurad Saparov,⁵ Yoshiyuki Ohtsubo,⁶ Tian Qian,¹ Athena S. Sefat,⁵ Silke Biermann,^{2,7,8} and Hong Ding^{1,3}

¹Beijing National Laboratory for Condensed Matter Physics, and Institute of Physics, Chinese Academy of Sciences, Beijing 100190, China

²Centre de Physique Théorique, Ecole Polytechnique, CNRS, Université Paris-Saclay, 91128 Palaiseau, France

³Collaborative Innovation Center of Quantum Matter, Beijing, China

⁴Swiss Light Source, Paul Scherrer Institut, CH-5232 Villigen PSI, Switzerland

⁵Materials Science and Technology Division, Oak Ridge National Laboratory, Oak Ridge, Tennessee 37831-6114, USA

⁶Synchrotron SOLEIL, Saint-Aubin-BP 48, F-91192 Gif sur Yvette, France

⁷Collège de France, 11 place Marcelin Berthelot, 75005 Paris, France

⁸European Theoretical Synchrotron Facility, Europe

(Received 14 May 2015; revised manuscript received 28 May 2016; published 20 June 2016)

We present a study of the tetragonal to collapsed-tetragonal transition of CaFe_2As_2 using angle-resolved photoemission spectroscopy and dynamical mean field theory-based electronic structure calculations. We observe that the collapsed-tetragonal phase exhibits reduced correlations and a higher coherence temperature due to the stronger Fe-As hybridization. Furthermore, a comparison of measured photoemission spectra and theoretical spectral functions shows that momentum-dependent corrections to the density functional band structure are essential for the description of low-energy quasiparticle dispersions. We introduce those using the recently proposed combined “screened exchange + dynamical mean field theory” scheme.

DOI: [10.1103/PhysRevB.93.245139](https://doi.org/10.1103/PhysRevB.93.245139)

I. INTRODUCTION

CaFe_2As_2 at ambient pressure and temperature is in a paramagnetic tetragonal phase. When temperature is lowered under 170 K it develops a collinear antiferromagnetic order and becomes orthorhombic [1–3]. Under pressure, this orthorhombic phase can be suppressed and replaced by a nonmagnetic collapsed-tetragonal phase in which the distance between two FeAs layers is strongly reduced due to the formation of covalent bonds between As atoms from two different layers. Superconductivity can develop from this collapsed phase [4,5]. Recently, it has been found that a quench during crystal synthesis can produce samples presenting similar properties as CaFe_2As_2 under pressure [6,7]. At ambient temperature and pressure, they are in the tetragonal phase, and when temperature is lowered there is a transition into a collapsed-tetragonal phase, around 90 K in our samples [7]. There are also other ways to induce a collapse transition at ambient pressure, such as isovalent substitution of As by P [8], electron-doping by Rh at the Fe site [9], or electron doping by rare earth on the Ca site [10]. However, while CaFe_2As_2 in the collapsed-tetragonal phase can become superconductor under pressure¹ or with rare-earth doping [4,10,11], it is not the case in these quenched crystals.

During the collapse caused by increasing pressure, the c axis of the unit cell is strongly reduced by about 9%–10%, while the a axis is enlarged by about 2%. In our samples, the transition is done by lowering temperature and the c axis is reduced by about 5%–6%. This modification of the crystal structure is at the origin of a reorganization

of the Fermi surface and electronic structure of the compound [8,9,12–14], which has been studied within density functional theory (DFT) [8,13,15,16] and very recently within combined density functional dynamical mean field theory (DFT+DMFT) [17,18]. The electronic structure of CaFe_2As_2 and of its different phases has also been probed by photoemission experiments [13,19,20]. In particular, it was found that the electronic correlations are reduced in the collapsed phase. Interestingly, the resistivity at the transition changes its low-energy behavior from $\rho \propto T$ or $\rho \propto T^{1.5}$ in the tetragonal phase to $\rho \propto T^2$ —as in a good Fermi liquid—in the collapsed-tetragonal phase [7,9,21]. In rare-earth electron-doped $\text{Ca}_{1-x}\text{RE}_x\text{Fe}_2\text{As}_2$, this Fermi-liquid-like resistivity at low temperatures is observed independently of the stable phase—collapsed-tetragonal or noncollapsed-tetragonal as in $\text{Ca}_{1-x}\text{La}_x\text{Fe}_2\text{As}_2$ [10]. Recent nuclear magnetic resonance data further indicate a suppression of antiferromagnetic spin fluctuations in the collapsed-tetragonal phase [22]. Motivated by these intriguing results, we have performed DFT+DMFT calculations and ARPES experiments on the tetragonal and collapsed-tetragonal phase of CaFe_2As_2 .

II. THE COLLAPSE TRANSITION AS SEEN BY ARPES

We have performed angle-resolved photoemission measurements on samples grown by the self-flux method that are quenched from 960 °C (corresponding to as-grown “p1” samples in Ref. [7]). Experiments were conducted at the CASSIOPEE beamline of SOLEIL synchrotron (France) and at the Institute of Physics, Chinese Academy of Sciences (China). Both systems are equipped with VG-Scienta R4000 electron analyzers. All samples were cleaved *in situ* at temperatures higher than 200 K and measured in a working vacuum between 5×10^{-10} and 1×10^{-9} torr at SOLEIL,

*vanroeke@cpht.polytechnique.fr

¹Superconductivity can also occur in a noncollapsed phase, e.g., in $\text{Ca}_{1-x}\text{La}_x\text{Fe}_2\text{As}_2$ [10] or for low-doping values in $\text{CaFe}_2\text{As}_{2-x}\text{P}_x$ [21].

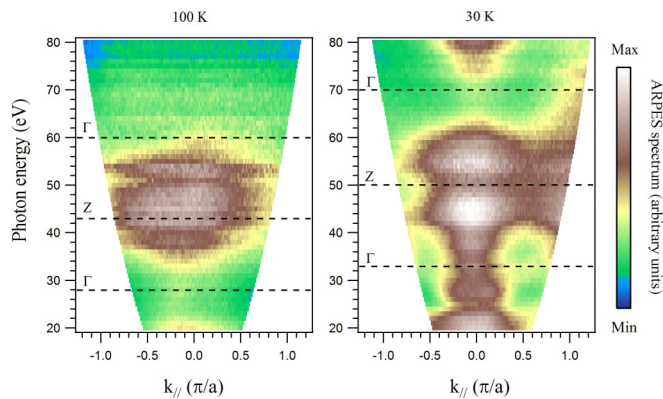


FIG. 1. Photon energy dependence of the ARPES spectra of CaFe_2As_2 in the tetragonal ($T = 100$ K) and collapsed-tetragonal ($T = 30$ K) phases at the Fermi level around the Γ point.

and better than 5×10^{-11} torr at the Institute of Physics. The photon energy was varied from 20 to 80 eV in synchrotron while we used the He α line of an helium discharge lamp in the laboratory (21.218 eV). The angular resolution was better than 0.5° and the energy resolution better than 10 meV.

Samples were measured at 200, 100, 80, and 30 K. The tetragonal to collapsed-tetragonal transition is shown to occur around 90 K by our magnetic susceptibility measurements, with a hysteresis smaller than 5 K, in agreement with Ref. [7]. Although we have performed the temperature-dependent measurements at the Institute of Physics, the Fermi surfaces obtained in SOLEIL are similar to those obtained in our laboratory, indicating that the measured samples are in the same phase.

Figure 1 displays the photoemission spectra centered on the Γ point at the Fermi level for different photon energies, in the collapsed-tetragonal and tetragonal phases. From the observed periodicity of the spectrum in the collapsed-tetragonal phase we find that the Γ point is located around 33 and 70 eV, whereas a Z point is found around 50 eV. Using the sudden approximation and nearly free-electron model for the final state: $k_\perp = \sqrt{2m(E_{\text{kin}} \cos^2 \theta + V_0)}/\hbar$ and the lattice parameters of Saporov *et al.* [7], we deduce an inner potential V_0 of about 15 eV, which is consistent with other Fe-based superconductors [23]. This value of the inner potential also corresponds well to the data observed by Dhaka *et al.* [13]. In the tetragonal phase the data are less clear, but using the same value for V_0 we estimate the Γ point to be around 28 and 60 eV and the Z point around 43 eV. This assumption is plausible at 28 eV, even though for higher photon energy there seems to be a slight discrepancy with the observed spectrum. This might be due to a modification of the inner potential since the surface will probably be different in the tetragonal phase.

Figure 2 shows the Fermi surface of our CaFe_2As_2 sample in the tetragonal and collapsed-tetragonal phases recorded with a photon energy of 21.218 eV. We have lowered the temperature from 200 to 30 K and finished the measurements less than 30 h after the cleave, such that the aging of the sample was not important. Using the previously deduced inner potential, we

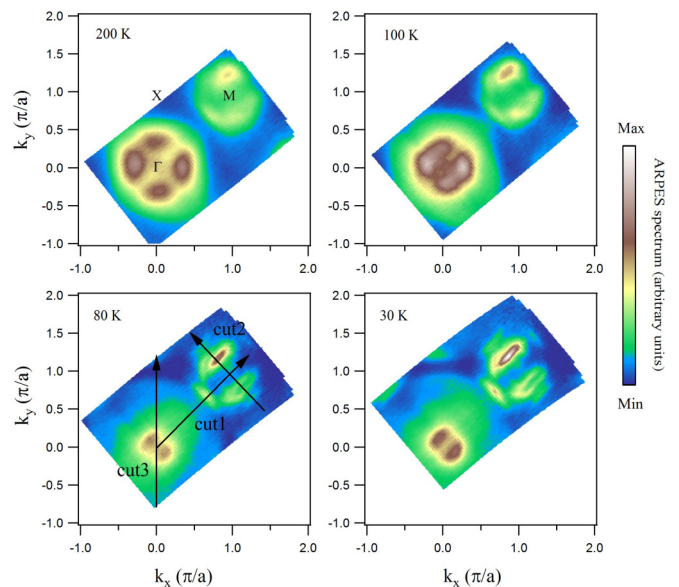


FIG. 2. Fermi surface mapping of CaFe_2As_2 in the tetragonal ($T > 90$ K) and collapsed-tetragonal ($T < 90$ K) phases.

find that for the collapsed-tetragonal phase the Γ point² has a k_z close to $1.25\pi/c'$ —with $c' = c/2$ the distance between two FeAs layers, close to the Z point of coordinates $(0, 0, \pi/c')$. k_z then decreases when k_\parallel is increased, with a value of $0.89\pi/c'$ at the M point and $1.01\pi/c'$ at the X point. It is interesting to note that the point symmetric to Γ with respect to the X point would have for coordinates $(2\pi/a, 0, 0.5\pi/c')$, such that it would nearly correspond to the same high-symmetry point.³ For the tetragonal phase, we find $k_z = 1.6\pi/c'$ at the Γ point and $k_z = 1.19\pi/c'$ at the M point.

For a more detailed analysis of the states forming the Fermi surface, we also present three different cuts. We first show the Γ - M direction for all temperatures (see Fig. 3 for the spectra and its curvature [24]). We also display a cut near the M point on the direction perpendicular to Γ - M (see Fig. 4, left panel) and another one along the Γ - X direction (Fig. 4, right panel), for the collapsed-tetragonal phase at 80 K only (similar results are obtained at 30 K). In the tetragonal phase, we can distinguish two hole-like bands forming circular hole pockets near the Γ point, although one may not cross the Fermi level. We also find two electron pockets around the M point. This is similar to what is found in many iron pnictides, and in particular in BaFe_2As_2 . Below the transition temperature, the Fermi surface is reorganized. The circular hole pocket around the Γ point shrinks drastically—or even disappears—while a large square hole pocket develops. This shape of the hole-like bands is very characteristic of the collapsed structure and qualitatively different from what is seen in BaFe_2As_2 [25]. This effect is due to a stronger three-dimensional character, as can be observed from the photon-energy-dependent data

²For simplicity, we name the points measured in Fig. 2 as their projection on the $k_z = 0$ plane.

³Indeed, the point Z with coordinates $(0, 0, \pi/c')$ is equivalent to the point with coordinates $(2\pi/a, 0, 0)$.

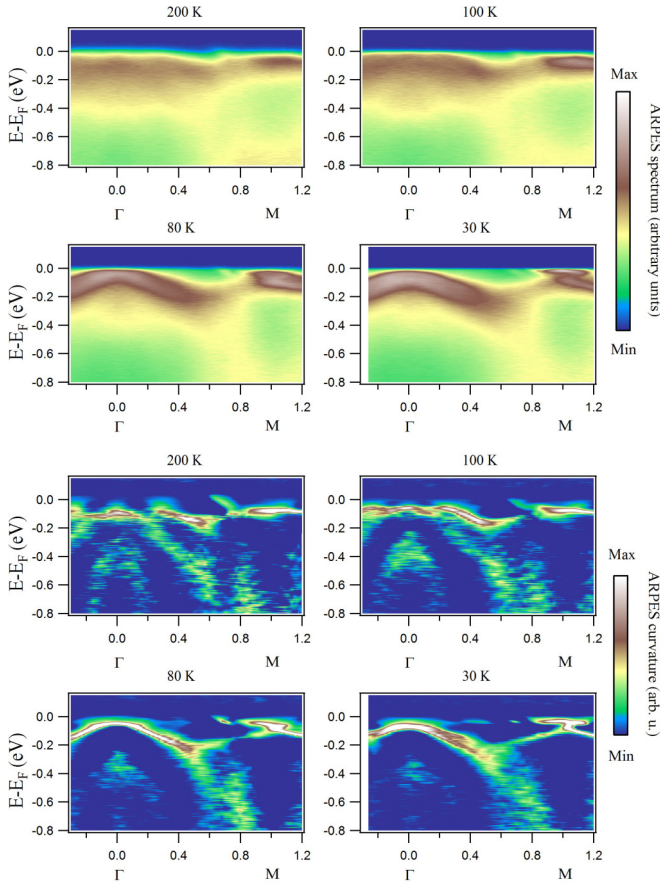


FIG. 3. ARPES spectra (top) and curvature (bottom) of CaFe_2As_2 in the tetragonal ($T > 90$ K) and collapsed-tetragonal ($T < 90$ K) phases along cut 1 of Fig. 2.

of Fig. 1. Indeed, the k_z dispersion is enhanced by the strong As-As p_z interlayer hybridization in the collapsed phase. On the other hand, the electron pockets near M keep a similar size.

From the temperature-dependent photoemission spectra of Fig. 2, it is interesting to see how the features become better defined as temperature is lowered. Notably, there is a clear difference between spectra above (at 100 K) and below (at 80 K) the collapse transition. However, because the quasiparticle dispersions are also changed through this transition, and because overall the spectrum appears to be very sensitive to temperature, it is difficult to attribute this improvement to the transition only.

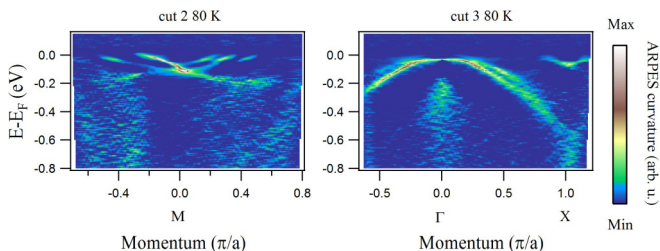


FIG. 4. Curvature of the ARPES spectra of CaFe_2As_2 in the collapsed-tetragonal phase ($T < 90$ K) along cut 2 (near the M point, left) and along cut 3 (right) of Fig. 2.

III. DFT+DMFT CALCULATIONS

We now turn to a theoretical description of the spectral properties of CaFe_2As_2 , using *first principles* dynamical mean field theory (DMFT) techniques. The first step are calculations based on the by now well-established DFT+DMFT method [26,27]. We use the DFT+DMFT implementation of Ref. [28] within the local density approximation (LDA) to the exchange-correlation functional, and Hubbard and Hund's interactions obtained from the constrained random phase approximation (cRPA) [29] in the implementation of Ref. [30]. The cRPA calculations yield $F^0 = 2.5$ eV, $F^2 = 6.0$ eV, and $F^4 = 4.5$ eV, corresponding to a Hund's rule coupling of $J = 0.75$ eV. Those values are valid indifferently for the collapsed and noncollapsed phase, since the differences between the computed values are of the order of 0.01 eV.

Figure 5 shows the momentum-resolved spectral function calculated from DFT+DMFT. Comparing the two phases one remarks a rearrangement of the Fermi surface at Γ reminiscent of the one observed in experiment: two hole pockets sink below the Fermi surface, and only the d_{xy} hole pocket remains. The dispersion of the bands with respect to k_z also increases, due to the As-As interlayer hybridization. This leads to an enhanced three-dimensional structure of the Fermi surface, but also to a modification of the two d_{z^2} bands that are around -0.5 eV at the Γ point and display an enhanced splitting around the Z point. Finally, we note that the size of the d_{xy} electron pocket at the M point is importantly reduced, and this compensates the suppression of the hole pockets. Those effects are also visible in the momentum-integrated spectral function (Fig. 6): indeed, we observe a reduction of the density of states at the Fermi level in the collapsed tetragonal phase due to the stronger dispersion leading to the suppression of the pockets.

Finally, we analyze the many-body self-energy calculated from DFT+DMFT. This quantity is plotted—in an orbital-resolved manner—in Fig. 7. The left panel represents the self-energy on the imaginary frequency (Matsubara) axis, the right panel gives its analytically continued version. The latter can be interpreted as the inverse lifetime of one-particle excitations at the given frequency. One clearly notices the quick decrease of the lifetime when moving away from the Fermi level. Without surprise, the orbitals that are nearly “gapped” around the Fermi level, the $x^2 - y^2$ and the z^2 are more coherent, and coherence improves in the collapsed phase as compared to the tetragonal one. This effect is accompanied by effective masses that are also more strongly enhanced in the tetragonal phase as compared to the collapsed one, as seen from Table I. These findings are in agreement with Refs. [17,18].

TABLE I. Mass renormalizations calculated from DFT+DMFT for the Fe-3d orbitals.

	d_{z^2}	$d_{x^2-y^2}$	d_{xy}	d_{xz+yz}
Tetragonal	1.43	1.37	1.64	1.57
Collapsed-tetragonal	1.35	1.36	1.45	1.46

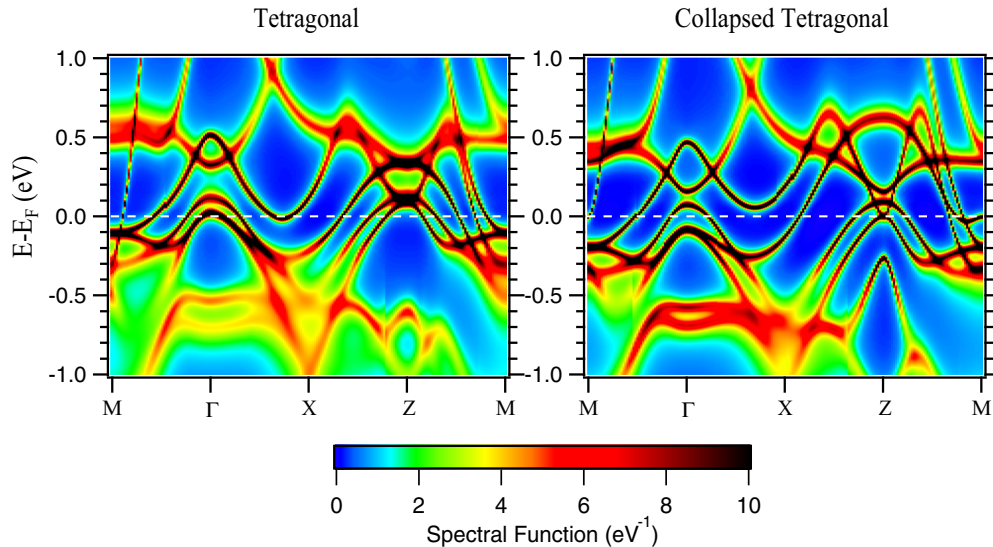


FIG. 5. Momentum-resolved DFT+DMFT spectral function for the tetragonal and tetragonal collapsed phases of CaFe_2As_2

In order to be able to make a more detailed comparison between theoretical and experimental spectra, Fig. 8 presents the superposition of bands extracted from DFT+DMFT calculations performed at 120 K with the ARPES spectrum along the Γ - M direction. We have taken into account the variation of k_z as indicated previously. Overall, the band renormalization is correctly described by the DFT+DMFT calculations. The theoretical quasiparticle renormalizations as extracted from a linearization around the Fermi energy of the imaginary part of the self-energy on the Matsubara axis are displayed in Table I. A caveat is, however, in order since the linear regime is really restricted to the first few Matsubara frequencies only, indicating that at the temperature of the calculation the system is at the border to an incoherent regime. Interestingly, on larger energy scales, at least in the tetragonal phase the self-energy can quite well be fitted by a power law behavior ω^α with α around 0.75. This is reminiscent to what was found in BaFe_2As_2 in Ref. [31].

We can also see from the calculations that there may be three hole-like bands in total in the tetragonal phase but two are nearly degenerate near the Γ point. However, if we look at the precise details of the low-energy states, we can find several discrepancies. In the tetragonal phase at the Fermi level, one of the bands near the Γ point is not well described. It is not clear if this is due to possible surface effects, limitations of the calculations, or other issues. On the other hand, the electron pockets are well described. In the collapsed-tetragonal phase, the two hole-like bands near the Γ point appear to be very close to each other from photoemission measurements, as can be seen even more clearly on the 30 K data of Fig. 3 and along the Γ - X direction of Fig. 4. At the M point, two bands are responsible for the electron pockets; however, the shape deviates from the experimental data due to upbending of one of the bands. On the other hand, we consider the agreement for the Fermi vector of the large hole pocket relatively satisfying since this band is very sensitive to the precise value of k_z .

If we suppose that the ARPES spectrum reflects the bulk features of the collapsed-tetragonal phase, an important test for

improved calculational schemes will be the correct prediction of the dispersion of the two hole-like bands near Γ , and of the interesting topology found near the M point in Fig. 4, which shows three bands crossing the Fermi level very close to each other—one of them being the large hole pocket. This last point is very specific to this compound in the iron pnictides family and due to the large k_z dispersion of the collapsed phase. We will present results beyond current DFT+DMFT techniques for CaFe_2As_2 in Sec. V.

IV. INTERPLAY OF STRUCTURAL AND ELECTRONIC PROPERTIES WITHIN DFT+DMFT: INTERLAYER VERSUS INTRALAYER GEOMETRIES

The origin of the reduction of correlations in the collapsed-tetragonal phase compared to the tetragonal phase is challenging to understand since both Fe-As and As-As bindings are modified. Indeed, in the collapsed structure the As-As interlayer binding is much stronger, which should increase the three-dimensional character of the band structure dispersion. However, the transition has also another effect on the Fe-As binding since the c axis collapses so much that the As height to the Fe plane is reduced. The result is that the Fe-As distance is shortened, suggesting an enhancement of the hybridization between the As- $4p$ and the Fe- $3d$ orbitals—though the expansion of the a axis limits this enhancement.

To decouple these two effects we have performed DFT+DMFT calculations on two hypothetical “hybrid” compounds. In the first one, we keep the same angle and distances between atoms within the FeAs layers as in the tetragonal phase, while the interlayer As-As distance is that of the collapsed-tetragonal phase. In the other one, we do the opposite: the layer is that of the collapsed-tetragonal phase and the interlayer distance is that of the tetragonal phase.

The imaginary part of the self-energy of the d_{xy} orbital in Matsubara frequencies is displayed in Fig. 9. The effect on the $d_{xz} + d_{yz}$ orbital is similar, and since those orbitals have the highest density-of-states at the Fermi level, we expect that

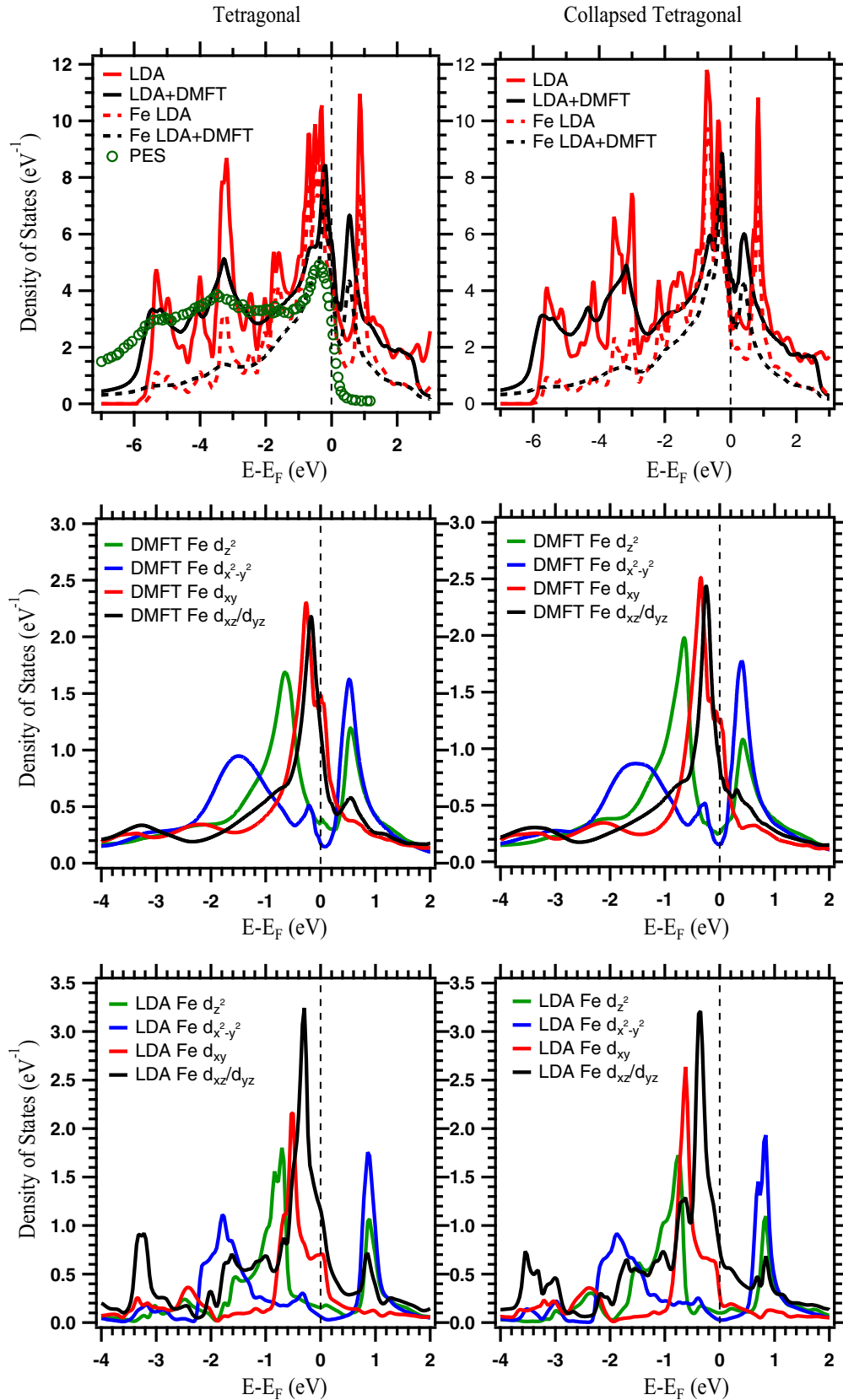


FIG. 6. DFT+DMFT spectral function ($U = 2.5$ eV, $J = 0.75$ eV) and DFT DOS for the tetragonal and tetragonal collapsed phases of CaFe_2As_2 . The photoemission spectrum of the tetragonal phase at 300 K from Ref. [19] is also shown for comparison.

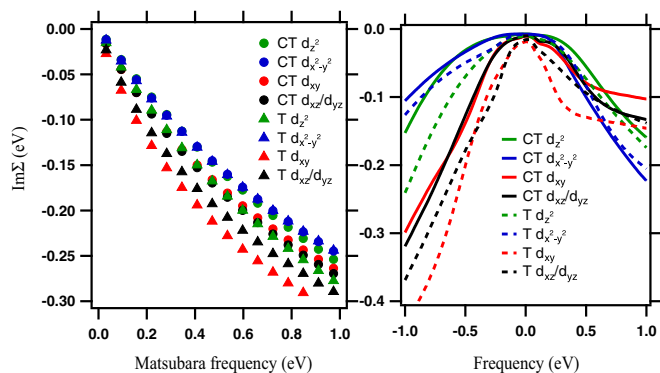


FIG. 7. Imaginary part of the DFT+DMFT self-energy for the tetragonal and tetragonal collapsed phases of CaFe_2As_2 .

they control the coherence properties of the compound.⁴ We can first see that in the collapsed phase the imaginary part of the self-energy displays a more coherent behavior, which corresponds to the longer lifetime of quasiparticles displayed in Fig. 8. Furthermore, the shape of the self-energy of the hybrid compounds depends on the structure of the FeAs layer, while it is nearly insensitive to the interlayer As-As distance. Naturally, in reality those two effects are linked with each other, since the deformation of the FeAs layer is caused by the

⁴In contrast, there is no difference between the four structures for the $d_{x^2-y^2}$ orbital and a much smaller one for the d_{z^2} orbital.

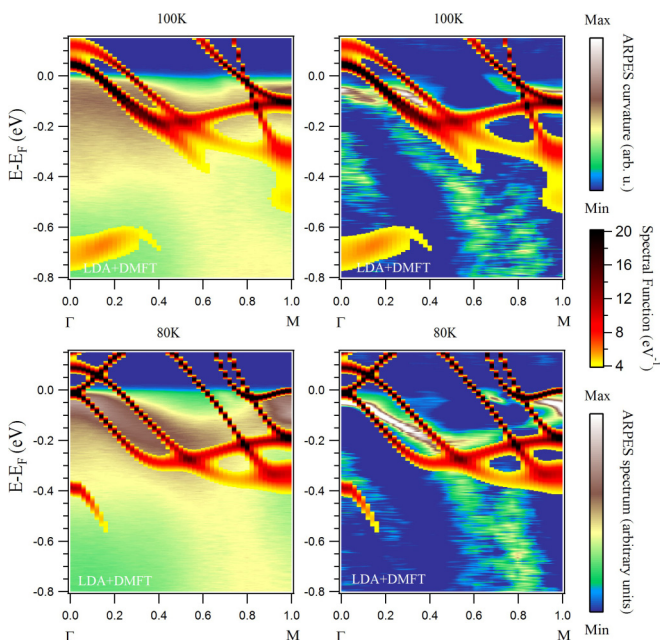


FIG. 8. Comparison of DFT+DMFT spectral functions with ARPES spectra of CaFe_2As_2 in the tetragonal and collapsed-tetragonal phases. The parts of the spectral functions with value higher than 4eV^{-1} are superimposed on the ARPES data of CaFe_2As_2 in the tetragonal (100 K) and collapsed-tetragonal (80 K) phases along the Γ - M direction, represented using the (left) spectra or (right) curvature.

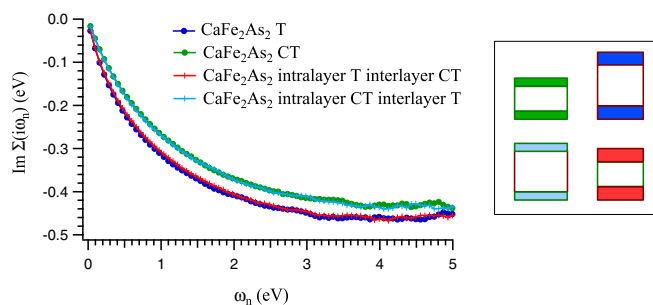


FIG. 9. Imaginary part of the self-energy in Matsubara frequencies of the d_{xy} orbital for CaFe_2As_2 in the tetragonal structure (T), collapsed-tetragonal structure (CT) and in two hypothetical structures mixing the interlayer (i.e., As-As interlayer distance) and intralayer (i.e., intralayer Fe and As angles and distances) of the tetragonal and collapsed-tetragonal structures. The inset shows a schematic view of the different structures (colors correspond to the legend).

formation of As-As bonds that make the c axis collapse. Still, this numerical experiment indicates that within DFT+DMFT the improvement of coherence properties is not due to the interlayer As-As bonding but to the increase of the Fe-As hybridization within a single layer.

V. BEYOND DFT+DMFT: RESULTS FROM SCREENED-EXCHANGE DYNAMICAL MEAN FIELD THEORY

Recently, a new calculational scheme that goes beyond current DFT+DMFT techniques was proposed [32,33]: the combination of a screened exchange Hamiltonian with “dynamical DMFT,” i.e., DMFT extended to dynamical Hubbard interactions [31,34,35], was shown to drastically improve upon the low-energy description of BaCo_2As_2 . In this context, the apparent success of the standard DFT+DMFT scheme was shown to result from an error cancellation effect: a one-body Hamiltonian where the local exchange-correlation potential of DFT has been replaced by a nonlocal screened Fock term has in fact a wider band structure than the DFT one, but including dynamical screening effects at the level of the Hubbard interactions leads to additional renormalizations of the electronic states, as compared to usual DMFT. For this

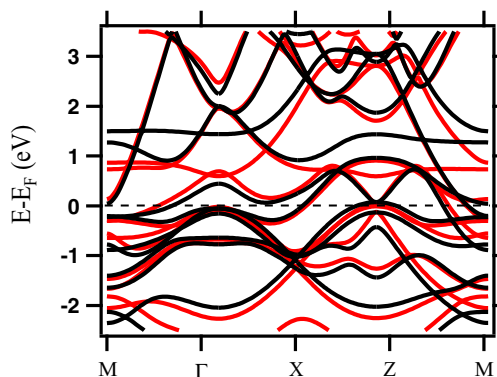


FIG. 10. Band structure of CaFe_2As_2 (collapsed tetragonal phase) within LDA (red) and screened exchange (black).

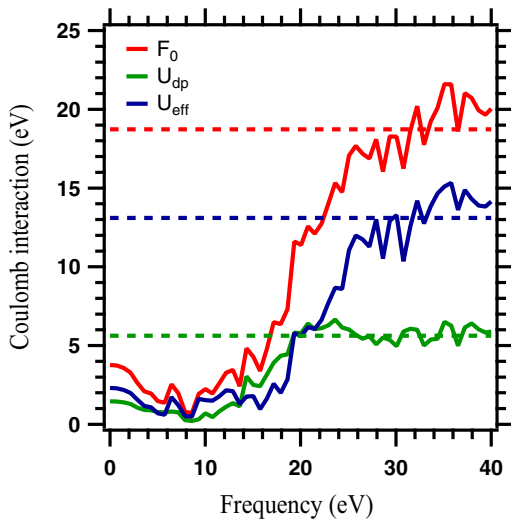


FIG. 11. Frequency-dependent Hubbard interaction for CaFe_2As_2 (collapsed tetragonal phase).

reason, the overall bandwidth of LDA+DMFT calculations and ‘screened exchange+dynamical DMFT’ (‘SEX+DDMFT’) calculations are similar. The low-energy dispersions are, however, quite strongly improved by the introduction of the nonlocal screened exchange contribution.

In Fig. 10, we present a comparison of the LDA band structure with the one obtained from screened exchange. The most obvious effect is the substantial band widening as expected and already analyzed for other compounds [32,33]. Beyond this trivial effect, more subtle rearrangements are observed around the Fermi level. Consistently with the increased bandwidth, the band closest to the Fermi level is pushed slightly down at the Γ point and symmetrically pushed up at the Z point. More interestingly, the d_{xy} band, that had nearly the same energy as the d_{xz}/d_{yz} band at the Z point, is now pushed down. Finally,

the shape of the smallest empty band close to the M point is modified along the ZM direction, suppressing the inflexion point close to M .

Figure 11 shows the frequency-dependence of $\mathcal{U}(\omega)$ as calculated from the cRPA and used in the SEX+DDMFT calculations described below. The overall shape resembles the familiar frequency-dependence already observed in other pnictide compounds [31,32]: at low frequencies, the (partially) screened value of 3.8 eV is read off. At high-frequencies, $\mathcal{U}(\omega)$ goes to the unscreened value of about 20 eV. The crossover happens at a characteristic plasma frequency of about 20 eV. Figure 11 shows not only the raw data as obtained within cRPA for a Hamiltonian with correlated d and p states, leading to dd , pp , and dp interactions, but also the effective shell-folded interaction (following the recipe of Ref. [36]) used in the SEX+DDMFT calculations. The shell-folding reduces the effective F^0 to 2.3 eV. It also mildens the frequency-dependence somewhat, but the overall variation of \mathcal{U} remains substantial. Finally, we use an orbital-dependent around-mean-field double counting [32].

In Fig. 12, we present the results of this SEX+DDMFT scheme, in the implementation of Ref. [32], applied to CaFe_2As_2 . We use the frequency-dependent interactions as calculated in Ref. [36] and a value of $\lambda = 1.7a_0^{-1}$ for the screening wavelength, which corresponds to the density-of-states at the Fermi level of the calculated result. As anticipated, due to the antagonistic effects of the nonlocal screened-exchange and of the high-frequency tail of the interactions, the overall renormalization of SEX+DDMFT is similar to the DFT+DMFT one. Still, the details of the quasiparticles dispersions at low energy are importantly modified. At the Γ and Z point, we observe the same differences as between the raw LDA and SEX band structures in which the d_{xy} band is pushed down by the nonlocal exchange. This has crucial effects on the Fermi surface, since now the last subsisting hole pocket at the Γ point has been suppressed, and the hole pocket close to the Z point is not of d_{xy} character but of d_{xz}/d_{yz} character.

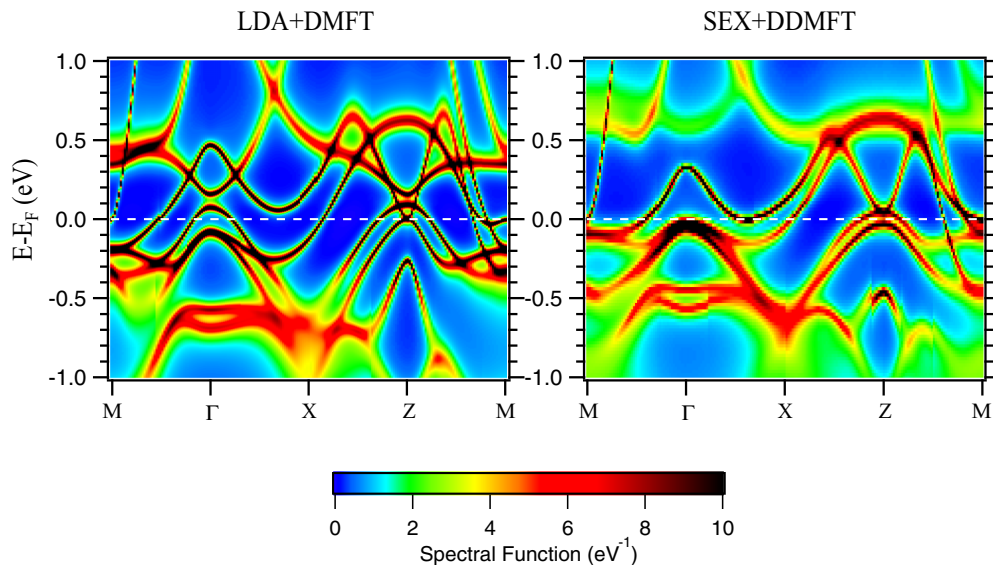


FIG. 12. Spectral function of CaFe_2As_2 (collapsed tetragonal phase): comparison of LDA+DMFT and SEX+DDMFT.

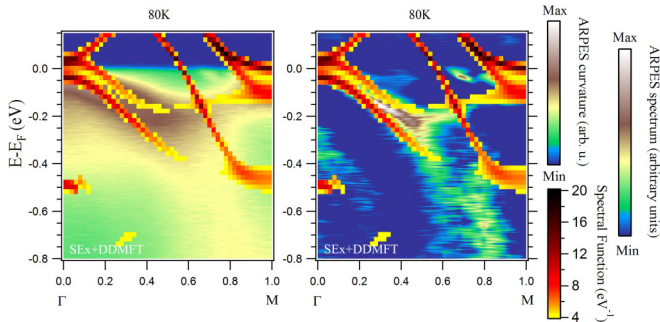


FIG. 13. Comparison of SEx+DDMFT spectral function with ARPES spectra of CaFe_2As_2 in the collapsed-tetragonal phase. The parts of the spectral functions with a value higher than 4 eV^{-1} are superimposed on the ARPES data of CaFe_2As_2 along the Γ - M direction, represented using the (left) spectra or (right) curvature.

Also, at the M point the energies of the bands close to the Fermi level are modified by as much as 0.1 eV, two of them being pushed up around -0.1 eV instead of -0.2 eV , and one pushed down around -0.45 eV instead of -0.35 eV .

To ease the comparison with the experimental spectra, we plot the superposition of the ARPES spectra with the theoretical result also for the SEx+DDMFT calculation (see Fig. 13). In the collapsed-tetragonal phase of CaFe_2As_2 , the two bands observed near the Γ point are correctly described, in contrast to DFT+DMFT. Since we are close to the Z point, we actually observe that the relative position of the d_{xz} and of the d_{yz} bands and their dispersions are rightly captured by taking into account the nonlocal exchange term in combination with dynamical screening. The third large hole pocket is at variance with the calculations, but we stress that its precise Fermi vector is very sensitive on the value of k_z .

VI. CONCLUSION

We have performed a study of the tetragonal and collapsed-tetragonal phases of CaFe_2As_2 using ARPES and electronic structure calculations. Our results support the picture that within DMFT, the collapsed-tetragonal phase exhibits reduced

correlations and higher coherence temperature due to the higher Fe-As hybridization, in agreement with other studies [17, 18]. However, we note that the reduction of correlations that we observe does not result in a dramatic change in the electronic self-energy that could explain by itself the behavior seen by resistivity measurements. This is confirmed by the ARPES results in the sense that the quasiparticle lifetimes away from the Γ point do not seem to be strongly impacted by the transition. Around the Γ point itself the electronic states found by photoemission appear more coherent but their dispersion has been largely reshaped by the collapse of the crystal. Furthermore, the unconventional transport behavior observed in experiments might not be the result of a change in electronic coherence alone. The reconstruction of the Fermi surface and of the low-energy electronic dispersion might induce geometric effects via, e.g., the Fermi surface nesting or dimensionality. Finally, at the temperature where the T —or $T^{1.5}$ —behavior of the resistivity is observed, phonons likely also come into play.

ACKNOWLEDGMENTS

We acknowledge useful discussions with Véronique Brouet and we are grateful to Thomas Ayrat, Michel Ferrero, and Olivier Parcollet for support on the TRIQS toolkit [37]. We acknowledge SOLEIL for provision of synchrotron radiation facilities and we would like to thank François Bertran, Patrick Le Fèvre, and Amina Taleb for assistance in using the beamline CASSIOPEE. This work was supported by the Cai Yuanpei program, IDRIS/GENCI Orsay under Project No. t2015091393, the European Research Council under Project No. 617196, the NSF under Grant No. NSF PHY11-25915, MOST (Grants No. 2010CB923000, No. 2011CBA001000, No. 2011CBA00102, and No. 2012CB821403) and NSFC (Grants No. 10974175, No. 11004232, No. 11034011/A0402, No. 11234014, and No. 11274362) from China. The work at Oak Ridge National Laboratory was primarily supported by the US Department of Energy, Office of Science, Basic Energy Sciences, Materials Science, and Engineering Division.

-
- [1] F. Ronning, T. Klimczuk, E. D. Bauer, H. Volz, and J. D. Thompson, *J. Phys.: Condens. Matter* **20**, 322201 (2008).
 - [2] N. Ni, S. Nandi, A. Kreyssig, A. I. Goldman, E. D. Mun, S. L. Bud'ko, and P. C. Canfield, *Phys. Rev. B* **78**, 014523 (2008).
 - [3] S. O. Diallo, V. P. Antropov, T. G. Perring, C. Broholm, J. J. Pulikkotil, N. Ni, S. L. Bud'ko, P. C. Canfield, A. Kreyssig, A. I. Goldman, and R. J. McQueeney, *Phys. Rev. Lett.* **102**, 187206 (2009).
 - [4] M. S. Torikachvili, S. L. Bud'ko, N. Ni, and P. C. Canfield, *Phys. Rev. Lett.* **101**, 057006 (2008).
 - [5] A. Kreyssig, M. A. Green, Y. Lee, G. D. Samolyuk, P. Zajdel, J. W. Lynn, S. L. Bud'ko, M. S. Torikachvili, N. Ni, S. Nandi, J. B. Leão, S. J. Poulton, D. N. Argyriou, B. N. Harmon, R. J. McQueeney, P. C. Canfield, and A. I. Goldman, *Phys. Rev. B* **78**, 184517 (2008).
 - [6] S. Ran, S. L. Bud'ko, D. K. Pratt, A. Kreyssig, M. G. Kim, M. J. Kramer, D. H. Ryan, W. N. Rowan-Weetaluktuk, Y. Furukawa, B. Roy, A. I. Goldman, and P. C. Canfield, *Phys. Rev. B* **83**, 144517 (2011).
 - [7] B. Saparov, C. Cantoni, M. Pan, T. C. Hogan, W. Ratcliff II, S. D. Wilson, K. Fritsch, B. D. Gaulin, and A. S. Sefat, *Sci. Rep.* **4**, 4120 (2014).
 - [8] A. I. Coldea, C. M. J. Andrew, J. G. Analytis, R. D. McDonald, A. F. Bangura, J.-H. Chu, I. R. Fisher, and A. Carrington, *Phys. Rev. Lett.* **103**, 026404 (2009).
 - [9] M. Danura, K. Kudo, Y. Oshiro, S. Araki, T. C. Kobayashi, and M. Nohara, *J. Phys. Soc. Jpn.* **80**, 103701 (2011).
 - [10] S. R. Saha, N. P. Butch, T. Drye, J. Magill, S. Ziemak, K. Kirshenbaum, P. Y. Zavalij, J. W. Lynn, and J. Paglione, *Phys. Rev. B* **85**, 024525 (2012).

- [11] K. Gofryk, M. Pan, C. Cantoni, B. Saparov, J. E. Mitchell, and A. S. Sefat, *Phys. Rev. Lett.* **112**, 047005 (2014).
- [12] K. Tsubota, T. Wakita, H. Nagao, C. Hiramatsu, T. Ishiga, M. Sunagawa, K. Ono, H. Kumigashira, M. Danura, K. Kudo, M. Nohara, Y. Muraoka, and T. Yokoya, *J. Phys. Soc. Jpn.* **82**, 073705 (2013).
- [13] R. S. Dhaka, R. Jiang, S. Ran, S. L. Bud'ko, P. C. Canfield, B. N. Harmon, A. Kaminski, M. Tomić, R. Valentí, and Y. Lee, *Phys. Rev. B* **89**, 020511 (2014).
- [14] K. Gofryk, B. Saparov, T. Durakiewicz, A. Chikina, S. Danzenbächer, D. V. Vyalikh, M. J. Graf, and A. S. Sefat, *Phys. Rev. Lett.* **112**, 186401 (2014).
- [15] T. Yildirim, *Phys. Rev. Lett.* **102**, 037003 (2009).
- [16] M. Tomić, R. Valentí, and H. O. Jeschke, *Phys. Rev. B* **85**, 094105 (2012).
- [17] S. Mandal, R. E. Cohen, and K. Haule, *Phys. Rev. B* **90**, 060501 (2014).
- [18] J. Diehl, S. Backes, D. Guterding, H. O. Jeschke, and R. Valentí, *Phys. Rev. B* **90**, 085110 (2014).
- [19] G. Adhikary, D. Biswas, N. Sahadev, R. Bindu, N. Kumar, S. K. Dhar, A. Thamizhavel, and K. Maiti, *J. Appl. Phys.* **115**, 123901 (2014).
- [20] K. Maiti, [arXiv:1501.01097](https://arxiv.org/abs/1501.01097) (2015)
- [21] S. Kasahara, T. Shibauchi, K. Hashimoto, Y. Nakai, H. Ikeda, T. Terashima, and Y. Matsuda, *Phys. Rev. B* **83**, 060505 (2011).
- [22] Y. Furukawa, B. Roy, S. Ran, S. L. Bud'ko, and P. C. Canfield, *Phys. Rev. B* **89**, 121109 (2014).
- [23] P. Richard, T. Sato, K. Nakayama, T. Takahashi, and H. Ding, *Rep. Prog. Phys.* **74**, 124512 (2011).
- [24] P. Zhang, P. Richard, T. Qian, Y.-M. Xu, X. Dai, and H. Ding, *Rev. Sci. Instrum.* **82**, 043712 (2011).
- [25] T. Kondo, R. M. Fernandes, R. Khasanov, C. Liu, A. D. Palczewski, N. Ni, M. Shi, A. Bostwick, E. Rotenberg, J. Schmalian, S. L. Bud'ko, P. C. Canfield, and A. Kaminski, *Phys. Rev. B* **81**, 060507 (2010).
- [26] A. I. Lichtenstein and M. I. Katsnelson, *Phys. Rev. B* **57**, 6884 (1998).
- [27] V. I. Anisimov, A. I. Poteryaev, M. A. Korotin, A. O. Anokhin, and G. Kotliar, *J. Phys.: Condens. Matter* **9**, 7359 (1997).
- [28] M. Aichhorn, L. Pourovskii, V. Vildosola, M. Ferrero, O. Parcollet, T. Miyake, A. Georges, and S. Biermann, *Phys. Rev. B* **80**, 085101 (2009).
- [29] F. Aryasetiawan, M. Imada, A. Georges, G. Kotliar, S. Biermann, and A. I. Lichtenstein, *Phys. Rev. B* **70**, 195104 (2004).
- [30] L. Vaugier, H. Jiang, and S. Biermann, *Phys. Rev. B* **86**, 165105 (2012).
- [31] P. Werner, M. Casula, T. Miyake, F. Aryasetiawan, A. J. Millis, and S. Biermann, *Nat. Phys.* **8**, 331 (2012).
- [32] A. van Roekeghem, T. Ayrál, J. M. Tomczak, M. Casula, N. Xu, H. Ding, M. Ferrero, O. Parcollet, H. Jiang, and S. Biermann, *Phys. Rev. Lett.* **113**, 266403 (2014).
- [33] A. van Roekeghem and S. Biermann, *Europhys. Lett.* **108**, 57003 (2014).
- [34] M. Casula, A. Rubtsov, and S. Biermann, *Phys. Rev. B* **85**, 035115 (2012).
- [35] L. Huang and Y. Wang, *Europhys. Lett.* **99**, 67003 (2012)
- [36] P. Seth, P. Hansmann, A. van Roekeghem, L. Vaugier, and S. Biermann, [arXiv:1508.07466](https://arxiv.org/abs/1508.07466) (2015)
- [37] O. Parcollet, M. Ferrero, T. Ayrál, H. Hafermann, I. Krivenko, L. Messio, and P. Seth, *Computer Physics Communications* **196**, 398 (2015).